Results in Engineering 21 (2024) 101752

Contents lists available at ScienceDirect

Results in Engineering

journal homepage: www.sciencedirect.com/journal/results-in-engineering

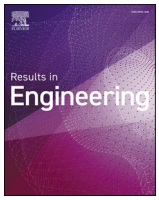

Graphene oxide boosted high surface area CeO_2 for humidity sensing

C Anjali [a], V Nidhisha [a], T.P Amrutha [a], Ritu Gopal [a], B Chethan [b], Mohamed Shahin Thayyil [c], Pradeepan Periyat [d], Renuka Neeroli Kizhakayil [a,*]

[a] Advanced Materials Research Centre, Department of Chemistry, University of Calicut, Kerala, 673 635, India
[b] Department of Physics, Indian Institute of Science, Bengaluru, Karnataka, 560012, India
[c] Department of Physics, University of Calicut, Kerala, 673635, India
[d] Department of Environmental Studies, Kannur University, 670567, India

ARTICLE INFO

Keywords:
Graphene oxide
Ceria
Humidity sensing
Response and recovery times
Stability

ABSTRACT

Precise measurement of humidity is of high significance in diverse fields like instrumentation, automated systems, agriculture and climatology. Herein as a first ever attempt, we report ceria-graphene oxide (CeO_2-GO) composites as resistive type humidity sensor, that shows attractive response to moisture. High surface area ceria is synthesised via ammonia mediated precipitation from salt precursor, and CeO_2-GO composites are achieved via hydrothermal route. The composites are well characterized using various analytical tools. Experiments using different mass ratios of GO in the composite show that there is an optimum amount of GO to realise maximum efficiency in the test parameters. It is further noted that the performance of the sensor is controlled by the active adsorption sites, which is proportional to surface area of the composite. An optimized CeO_2-GO matrix yielded a response and recovery time of 19 s and 10 s respectively. The narrow hysteresis in moisture adsorption-desorption study and excellent stability for about 60 days are also observed for the system, warranting the successful utility of the system for practical applications.

1. Introduction

Sensors are devices that make some detectable output signals upon interaction with a physical parameter, and they open up new applications and ways for better operational interactions [1]. Humidity sensors, focus of the present study, have been extensively used in various areas including medical field, industry, agriculture, food production etc., where utmost care is required for monitoring/controlling humidity [2]. The principle behind humidity sensors relies on converting the amount of water molecule in the environment in to a measurable signal. Humidity sensors can be categorized into resistance [3], capacitance [4], impedance, quartz crystal microbalance (QCM) resistance, surface acoustic wave (SAW) resistance, resonance type resistance [5] etc., in accordance with the change of physical parameters after interacting with water molecules. Spinels [6], oxides of transition metals and lanthanides [7–27] and pervoskite compounds [28,29] have been widely explored in the category of resistance type humidity sensors. Polymers [30–36], 2D materials such as MoS_2 [37–39], WS_2 [40–42], and black phosphorous [43–45] also fall in the category of materials explored to this effect. Various carbon materials such as porous carbon [46], carbon nano tube [47,48] and graphene [49,50] are also investigated for their response towards humidity. Out of the semi conducting materials explored, the interest in lanthanides, especially in cerium oxide, has increased recently, as it is economically competitive and abundant as copper oxides [51,52]. However, resistance type humidity sensors based on CeO_2 usually exhibit long response and recovery times, and fail to meet the requirements for onsite humidity detection [23]. This disadvantage is overcome by modifying ceria by suitable species, that eventually enhances the response to water molecules [53]. In the present work, this is affected by incorporating graphene oxide in ceria matrix.

The oxidised form of graphene, GO, has caught tremendous attention owing to its adorable properties [54], including water purification and humidity sensing [55]. Features like flexibility, transparency and super permeability to water bestow enhanced response to GO towards moisture. Graphene oxide supported on silicon wafer is utilised for colorimetric humidity sensing by the researchers [56]. It is noted that electrical type GO based humidity sensors show low conductivity and less moisture sensitivity due to the interruption of the conjugated electronic state in GO. Recent research shows better sensing and response and recovery times for GO as a capacitive type humidity sensor. The

* Corresponding author.
E-mail address: renuka@uoc.ac.in (R. Neeroli Kizhakayil).

https://doi.org/10.1016/j.rineng.2024.101752
Received 22 September 2023; Received in revised form 24 November 2023; Accepted 24 December 2023
Available online 5 January 2024

noble goal of this work is the setting up of a solid position for graphene oxide in resistive type humidity sensors. In this direction, CeO_2-GO nanocomposites achieved via simple hydrothermal process are examined for resistive type humidity sensing at room temperature. Fine dispersion of nano ceria in graphene oxide matrix tunes the response of the composites towards moisture favourably. CeO_2-GO composites of varying compositions are prepared and well characterised using various analytical tools. An optimized composition containing 7 wt % graphene oxide exhibited significantly low response and recovery times of 19 s and 10 s, in the respective order. This approach is scalable and financially viable, assuring successful utility of the material in commercial applications.

2. Materials and methods

2.1. Materials and reagents

The study employed materials and reagents including graphite powder (ACROS ORGANICS), Ammonium ceric nitrate ($(NH_4)_2Ce(NO_3)_6$, 99 % purity, SPECTROCHEM PVT LTD), Potassium permanganate, ($KMNO_4$, 99 % purity (SRL), and Ammonia solution ($NH_{3(aq)}$ 25 %, Merck), Solvents used in this research, Hydrochloric acid (HCl,37 %), Sulfuric acid (H_2SO_4,97 %), Hydrogen peroxide (H_2O_2, 30 %) and Phosphoric acid (H_3PO_4, 88 %) are sourced from Sigma Aldrich. All the solutions were prepared using Deionized (DI) water obtained using Aquoion TBD 50 Two Bed Demineraliser and hydrophilic graphene oxide were synthesised by following toxic gas free modified Hummers' method.

2.2. Synthesis procedures

2.2.1. Synthesis of graphene oxide

According to standard protocol, pure graphite powder was used to create graphene oxide (GO) using the modified Hummers process [57]. In this procedure, 27 mL of sulfuric acid (H_2SO_4) and 3 mL of phosphoric acid (H_3PO_4) were combined at a 9:1 vol ratio and stirred for a while. Next, the solution was supplemented with 0.225 g of graphite powder under maintaining the stirring.1.32 g of potassium permanganate ($KMnO_4$) was gradually added to the mixture. The solution turned dark green after 6 h stirring. 0.675 mL of hydrogen peroxide (H_2O_2) was added gradually and again agitated for 10 min in order to remove the excess $KMnO_4$. The endothermic nature of the process was associated with cooling. The mixture was centrifuged at 3000 rpm for 15 min with 10 mL hydrochloric acid and 30 mL DI water added. For the full elimination of salts and acids, the obtained residue was then washed again with 5 % HCl and hot DI water.GO solution was dried in a hot air oven at 80 °C for 24 h to obtain fine GO powder. Subjected to ultrasonication for 2 h to obtain the light brown uniform suspension of GO.

2.2.2. Preparation of CeO_2-GO nanocomposite

Generally speaking, there are two distinct methods for planning and managing the synthesis of graphene-based nanostructures. In the first method, the precursor salt adheres to the graphene matrix's surface, where nanoparticles are formed directly while their sizes and shapes are controlled (in situ growth); in the second method, as-prepared nanostructures are anchored/deposited therein (self-assembly approach). Here, CeO_2 nanoparticles atop graphene sheets were grown under regulated conditions using a straightforward, inexpensive, and one-step (in situ growth) hydrothermal technique [58]. Briefly,in the first step, CeO_2 nano particles were synthesised by adopting a high surface area method. The procedure is as follows. NH_4OH (28 %) was added dropwise over 15 min duration to a stirred $Ce(NO_3)_4$ solution (1.5 M) at 0 °C, followed by warming to room temperature.0.5 M Cerium ion concentration was then achieved by diluting the yellow homogenous solution with DI water. This mixture with initial pH 1.17 is treated with 25 mL of 2.0 M NaOH over the course of about 15 min at 85 °C (1.5 mL/min). The final pH after the addition was complete was 9.16. The as-prepared GO suspension was added to the afore-mentioned mixture with constantly stirring, and the stirring was continued for an additional hour. Then poured into a 100 mL Teflon-lined stainless steel autoclave tube, which was then subjected to 24-h hydrothermal treatment in an electric oven set to 180 °C. The autoclave was allowed to spontaneously cool to ambient temperature after the reaction was complete. The next step was to dry the product overnight in a vacuum at 60 °C, after multiple washes with de-ionized water and 100 % ethanol. The black colour powder eventually obtained was collected for the sensing studies. The same procedure is adopted to synthesise five different composites, adjusting the graphene oxide percentage. The composites were named as HCG1, HCG4, HCG7, HCG10 and HCG13, in accordance with the weight percentage of graphene oxide in the sample. The digits in the name signify the percentage of graphene oxide in the composite.

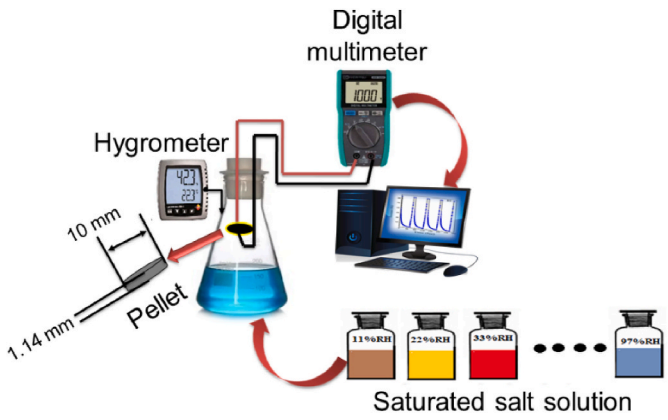

Fig. 1. Schematic of the humidity sensor experimental setup.

3. Characterization techniques

Several analytical tools provide a fair idea on the physicochemical features of the produced nano composite. Phase composition of the samples was analysed by X-Ray Diffraction using Rigaku Miniflex 600 diffractometer with a rotating anode. The Jasco FTIR-4100 spectrometer was used to record the FTIR spectra of the produced samples using the KBr disc method. Using the LabRam HR-Horiba Jobinyvon spectrometer, Raman spectral measurements were made. SEM-JSM 848 equipment and Philips CM 200 transmission electron microscope, respectively, were used for the samples' electron microscopic analysis (Scanning Electron Microscopy and Transmission Electron Microscopy). XPS analysis was made using AXIS-Supra + xps analyser in the region 200 -200eV. Utilizing the Brunauer Emmett and Teller (BET) method, the surface area measurements were performed using the Micromeritics Gemini surface area analyzer.

4. Humidity sensing measurements

The humidity measurements were carried out in a specially designed humidity chamber using pellet sample. Pellett of 1 mm thickness was prepared using a hydraulic press. Silver electrodes were pasted on the pellet to get the ohmic contact, and the pellet was held between the two probes of the specimen holder. Schematic of humidity sensing was illustrated in Fig. 1. The experimental setup was composed of saturated salt solutions in various flasks, each of which is kept at a specific RH percentage and measured using a humidity metre (make: Mextech-DT-615). The electrodes attached to the pellet run through a cork fitting at the top of each chamber and the sample was exposed to relative humidity in the reasonably, practically appropriate range of 11–97 %, and the variation in surface resistance was recorded before and after. The other ends of the electrodes were connected to a programmable

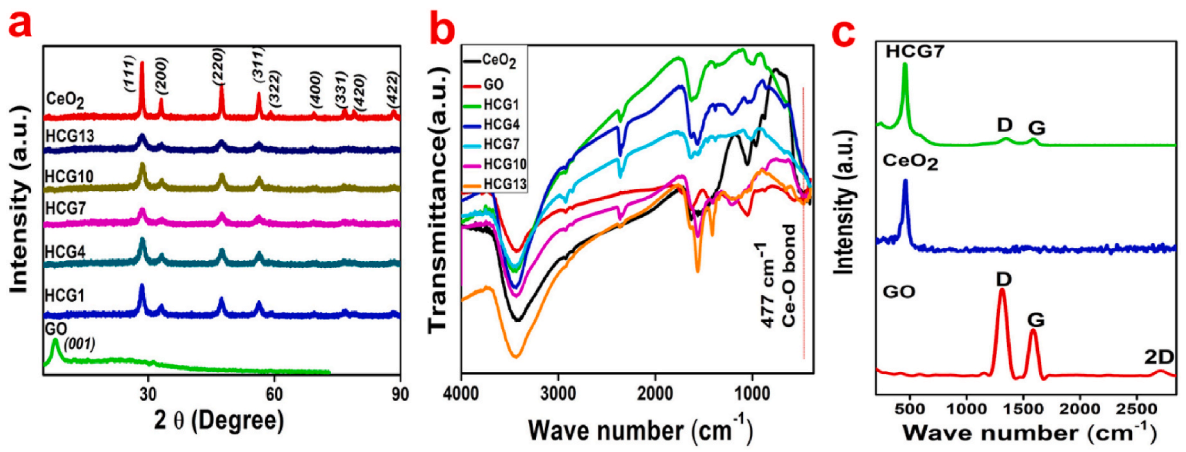

Fig. 2. a)XRD patterns and b) FTIR spectra of CeO_2, GO and the composites c) Raman spectrum of pure GO, CeO_2 and HCG7 system, containing 7 wt% GO.

computer interfaced digital multi metre (make: HIOKI, Japan, model: DT4282). The sensing response for each sample was computed using the following formula [59].

$$S_H = \frac{|R_{LH} - R_H|}{R_{LH}} \times 100\%$$

where, R_{LH} is the resistance of the sample at lower relative humidity and R_H is the resistance of the sample at higher relative humidity.

5. Results and discussion

5.1. Characterization of Ceria-GO composites

5.1.1. X-Ray Diffraction (XRD) analysis

The crystalline phase, purity and structural details of the as-synthesised composites are confirmed from the XRD pattern, depicted in Fig. 2a.From the figure, the most intense diffraction peak of GO can be marked at 2θ = 9.72°, which corresponds to a d-spacing of 0.90 nm, arising from the (001) reflection of graphite oxide.This d-spacing is noticeably larger than the d-spacing pure graphite (0.34 nm), showing that the flake-graphite was oxidised into graphite oxide, decorated by oxygen-containing functional groups, which results in an atomic-scale roughness.In the case of as-prepared CeO_2 nanoparticles,the XRD pattern validates the cubic fluorite-type structure of CeO_2 (JCPDS no. 34–0394), with peaks observed at 28.743°,33.04°,47.41°, 56.27°,58.96°,76.75°,79.04°and 88.32° 2θ,which are assigned to (111), (200),(220),(311), (322), (400), (331) and (422) planes respectively [60], which is suggestive of CeO_2 phase. In the case of CeO_2-GO nano composites, it is clear that the primary diffracted peaks are identical to those of the as-prepared CeO_2 nanoparticles. The broad peak for GO is not evident, in the composite. This is likely because the GO was wrapped in CeO_2 nanocrystals during the hydrothermal treatment or the strong peak of CeO_2 nanocrystals at around 28.74° at the (111) plane overwhelms the small peak of GO. Peaks of the composites were somewhat broader due to the presence of abundant functional groups on GO.

5.1.2. Fourier transform infrared spectroscopic (FT-IR) analysis

FT-IR spectroscopy is a non-destructive technique that yields the fingerprint of a sample with absorption peaks that correspond to the frequency of vibrations between different bonds in the material. The FT-IR spectra of CeO_2, GO and the CeO_2-GO nanocomposite are shown in Fig. 2b. The FT-IR spectra of GO shows distinctive absorption bands at 1735 cm^{-1} and 1059 cm^{-1}, which correspond to the C=O, and C–OH stretching vibrations of the COOH group, respectively. The band at 1642 cm^{-1} is attributed to the bending vibration of absorbed water molecules and the contributions of the sp^2 properties. The band noted at 1219 cm^{-1}accounts for the epoxy groups. The –OH stretching and deformation vibrations are responsible for the bands at around 3425 cm^{-1} and 1397 cm^{-1}, respectively [61]. FT-IR spectrum of CeO_2 shows a band at 477 cm^{-1} that corresponds to the Ce–O vibration of the CeO_2 crystal which confirms the formation of cerium oxide, and the band at 1622 cm^{-1} that is linked to the bending mode of hydroxyl group, may be caused by the presence of moisture in the sample [62]. CeO_2-GO nanocomposite contains the distinct bands of both CeO_2 and GO. A minor shift in Ce–O vibration position noted in the composites can be assigned to the strong interaction between CeO_2 nanoparticle and GO surface.

5.1.3. Raman analysis

Raman spectroscopy analysis is an important tool, that offers useful information on the electronic and structural characteristics of graphitic and graphene-related materials. Especially to identify the presence of defects, and order of crystal lattices, which are primarily reflected by the vibrational energies of the molecules. Raman spectrum GO, ceria and GO modified Ceria are presented in Fig. 2 (c). The three peaks in GO are attributed to the D band (1310 cm^{-1}), G band (1592 cm^{-1}) [63] and 2D band (2710 cm^{-1}). The D band is connected to structural flaws including bond-angle disorder, bond-length disorder, and hybridization that can violate the laws of symmetry and selection, while the G band is connected to in-plane vibration of sp^2 hybridised carbon atoms. The band ~2700 cm^{-1}, identified as the 2D band, serves as an indicator of number of layers in graphene. Strictly monolayer graphene exhibits a distinct sharp peak at approximately 2700 cm^{-1}. In this present case, the above-mentioned band is noted to be broadened, indicating the presence of few layer graphene, with some defects [64,65]. A slight shift in these bands are noted for the composite due to interaction with ceria, and are observed at 1349 cm^{-1} and 1548 cm^{-1}, in the respective order. The 2D band was absent in the composite. GO exhibits an I_D/I_G ratio 1.4, which is lowered to 1.13 for the composite. In the case of Raman spectra of pure-CeO_2 NPs, a strong peak at 466 cm^{-1}, corresponds to the symmetrical stretching vibrational mode of the Ce–O unit is seen, assigned to the F_{2g} transition [66]. This peak, which has a blue shift to 455 cm^{-1} in the CeO_2-GO nanocomposites, confirms the interaction between these moieties.

5.1.4. Field emission Scanning Electron Microscopy (FE-SEM)

In the FE-SEM images of CeO_2 nanoparticles instead of having a spherical ball shape, the CeO_2 nanoparticles morphology resembles that of crumpled up paper form, and their individual morphologies resemble ribbon shape. The method and conditions used during synthesis have a significant impact on the structure of the nanocomposite that is produced, as demonstrated by the ribbon-like CeO_2 nanoparticles we obtained using the high surface area ceria synthesis method. Micrometer

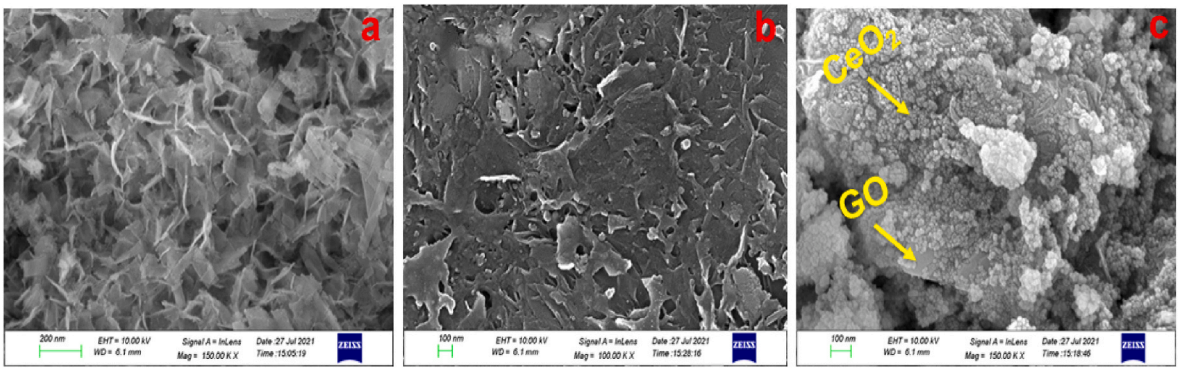

Fig. 3. SEM images of (a) CeO_2 (b) GO and (c) composite (HCG7).

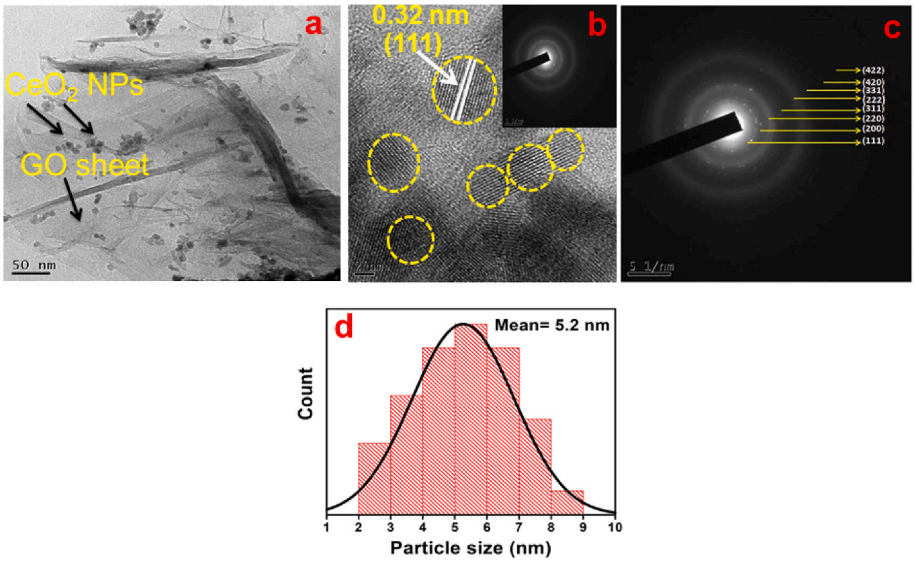

Fig. 4. (a) TEM image of CeO_2-GO nanocomposite shows the presence of CeO_2 NPs onto the graphene oxide matrix,(b) HR-TEM image showing lattice fringes of CeO_2NPs(c) SAED pattern showing hkl planes and (d) Particle size distribution curve obtained from HR-TEM.

dimension is presumed for the ceria system. GO shows the expected wrinkled and layered sheet-type morphology, as seen in the Fig. 3b.A regular distribution of ceria and graphene oxide is evident in the SEM image of CeO_2-GO nanocomposite (Fig. 3c). This demonstrates how well GO and CeO_2 nanoparticles combine. This combination not only effectively prevents the agglomeration of CeO_2 nanoparticles, but also hypothesised that the well-dispersed CeO_2 nanoparticles on the surfaces of the GOs may serve as spacers and prevent the GOs from restacking, increasing the stability of the single-or few-layer exfoliated GO.

5.1.5. *Transmission Electron Microscopy (TEM)*

Morphology and particle size of the as-produced CeO_2-GO nanostructures are studied by TEM tool (Fig. 4). Successful anchoring of CeO_2 NPs on graphene oxide surface is confirmed from the TEM image presented in Fig. 4a. Even distribution of metal oxide particles is seen on GO sheets. They demonstrated excellent interfacial contact between the graphene sheets and CeO_2 NPs. [67]. Additionally, most of the synthesised CeO_2 NPs are in the range, 4–8 nm, with spherical morphology, and finely dispersed over the graphene oxide sheets (Fig. 4b).

Individual nanoparticles showed an interplanar spacing of 0.32 nm, which is consistent with the (111) *d* spacing of CeO_2 phase, estimated from the XRD pattern. Fig. 4c shows the SAED pattern of the nanostructures with a series of bright rings, indicating that the sample is polycrystalline. The *d* spacing is also calculated from SAED pattern using image j software and is presented in Table 1. Fig. 4d shows the particle size distribution of ceria nanoparticles in the composite, as evident from the TEM image provided in Fig. 4a. The average size of these particles is estimated to be nearly 5.2 nm.

Table 1
d spacing and *hkl* values derived from SAED.

Sl.No.	1/2r (nm^{-1})	1/r (nm^{-1})	r (nm)	d spacing (Å)	(*hkl*)
1	6.112	3.056	0.3272	3.2722	(111)
2	8.81	4.405	0.2270	2.2701	(200)
3	11.984	5.992	0.1668	1.6688	(220)
4	15.161	7.5805	0.1319	1.3191	(311)
5	18.096	9.048	0.1105	1.1052	(222)
6	21.323	10.6615	0.0937	0.9379	(331)
7	23.254	11.627	0.0860	0.8600	(420)
8	25.794	12.897	0.0775	0.7753	(422)

5.1.6. *X-ray photoelectron spectroscopic analysis (XPS)*

Fig. 5depicts the XPS survey scan of the composite, in which the three peaks are attributed to Ce,O and peak of carbon (C1s). Within the sensitivity of the technique, no contamination peak was found. The binding energies (BE) of Ce 3 d^5,O 1s and C 1s were measured at 882.2 eV,531.2 eV and 283.5 eV respectively [68]. Four prominent peaks of ceria were clearly visible in the fitted spectra of the composite shown in Fig. 5b. Both Ceric and cerous forms of cerium are identified in the composite. The following Ce 3d peaks were confirmed by XPS analysis:

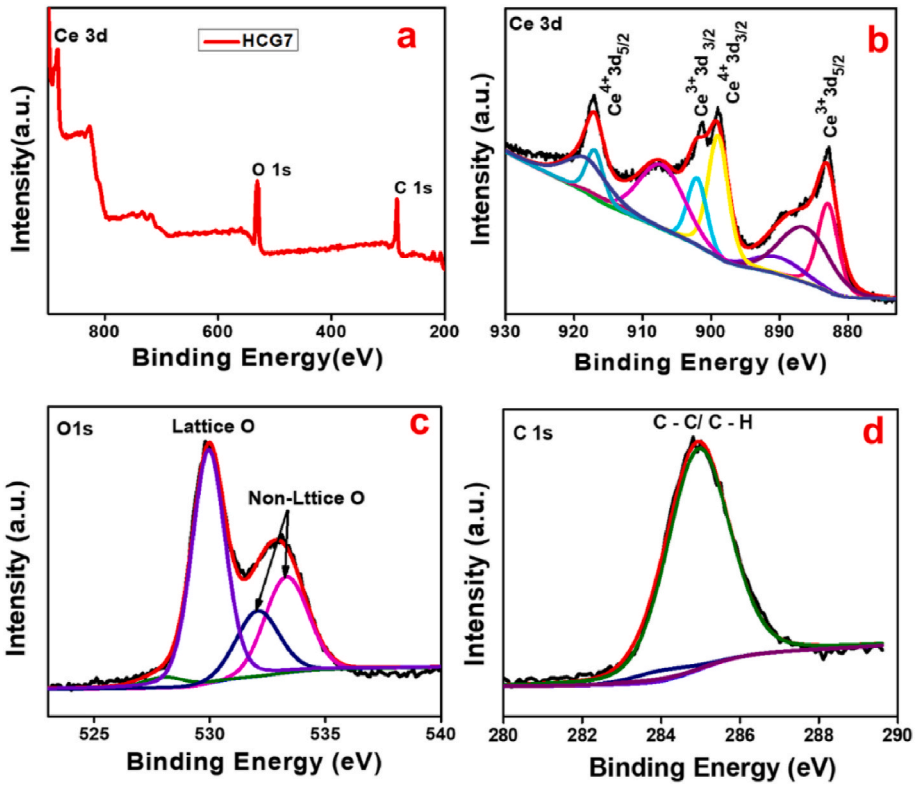

Fig. 5. (a) XPS survey scan of HCG7 system, containing 7 wt% GO, (b) Deconvoluted XPS region spectra of Ce 3d fitted spectra,(c-d) XPS fitting curve of O1s and C1s.

Table 2
Specific surface area measured from the BET analysis of the pure CeO_2 and the composites.

Sample name	BET surface area (m^2/g)
CeO_2	114.04
HCG1	127.51
HCG4	134.1
HCG7	147.18
HCG10	103.91
HCG13	54.70

Ce^{4+} $3d_{5/2}$, Ce^{3+} $3d_{3/2}$, Ce^{4+} $3d_{3/2}$, and Ce^{3+} $3d_{5/2}$. The primary characteristic peaks of Ce^{4+} $3d_{5/2}$ and Ce^{4+} $3d_{3/2}$ were seen at 916.7 and 898.4 eV, respectively. The peaks at 901.1 and 882.6 eV were attributed to Ce^{3+} $3d_{3/2}$ and $Ce^{3+}3d_{5/2}$, respectively. The spectral information is completely in agreement with earlier reports [69]. The C1s peak further curve fitting showed a peak at 284.35 eV indicative of C–C/C–H groups. No C=C was noted as per the XPS results. Highly oxygen functionalised graphene oxide of course rules out the possibility of unsaturated carbon framework. The peak at 285.31 eV, characteristic of C–O groups is also noted that can be ascribed to either surface OH functional groups or a C –O– Ce bond in the composite. Carbonyl/carboxyl groups were also not observed in the system.

5.1.7. *Specific surface area analysis by BET method*

Nitrogen adsorption via Brunauer-Emmett-Teller method was employed inorder to determine the specific surface area of the systems. BET specific surface area analysis were performed on pure CeO_2 and CeO_2-GO nanocomposites, and the results are depicted in Table 2.The special route adopted yielded ceria nanoparticles of high surface area when compared to systems yielded by usual methods. Graphene oxide incorporation substantially enhanced the surface area values up to HCG7. Thereafter a sharp decrease is seen for the surface area values. It is further noted that drastic reduction is seen in the values as the HO content is increased.

5.2. *Humidity sensing response*

The variation of resistance and sensing response of CeO_2 and the corresponding CeO_2-GO composites at room temperature in the RH range of 11–97 % is depicted in Fig. 7a&(c) respectively. It is obvious that there is a decrease in resistance with %RH of pure CeO_2 in the humidity range because the matching sensing response is only 30 %. However, resistance in the case of composites, investigated in the same RH range, has also phenomenally dropped linearly by four orders of magnitude. Additionally, as the amount of GO in the composites has increased, their sensing response has improved as well, reaching a maximum of 99.93 % for the HCG7 composite. BET surface area analysis showed that surface area of the composites increased uniformly with increasing the amount of GO in the composite, atributed to the presence of GO sheets, up to HCG7. SEM and TEM analysis show that CeO_2 particle are uniformly scattered over GO sheet and both the CeO_2 particles (Ce^{3+}& Ce^{4+}) and hydrophilic functional groups like hydroxyil, carboxyl and epoxy groups presents on the GO sheet simultaneously provide plentiful water-absorbing areas will enhance the sensing response of the composites [70]. The decisive role of surface area in humidity sensing application is already established.

The sensing mechanism observed in the composite can be explained by three consecutive processes—chemisorption, physiorption, and

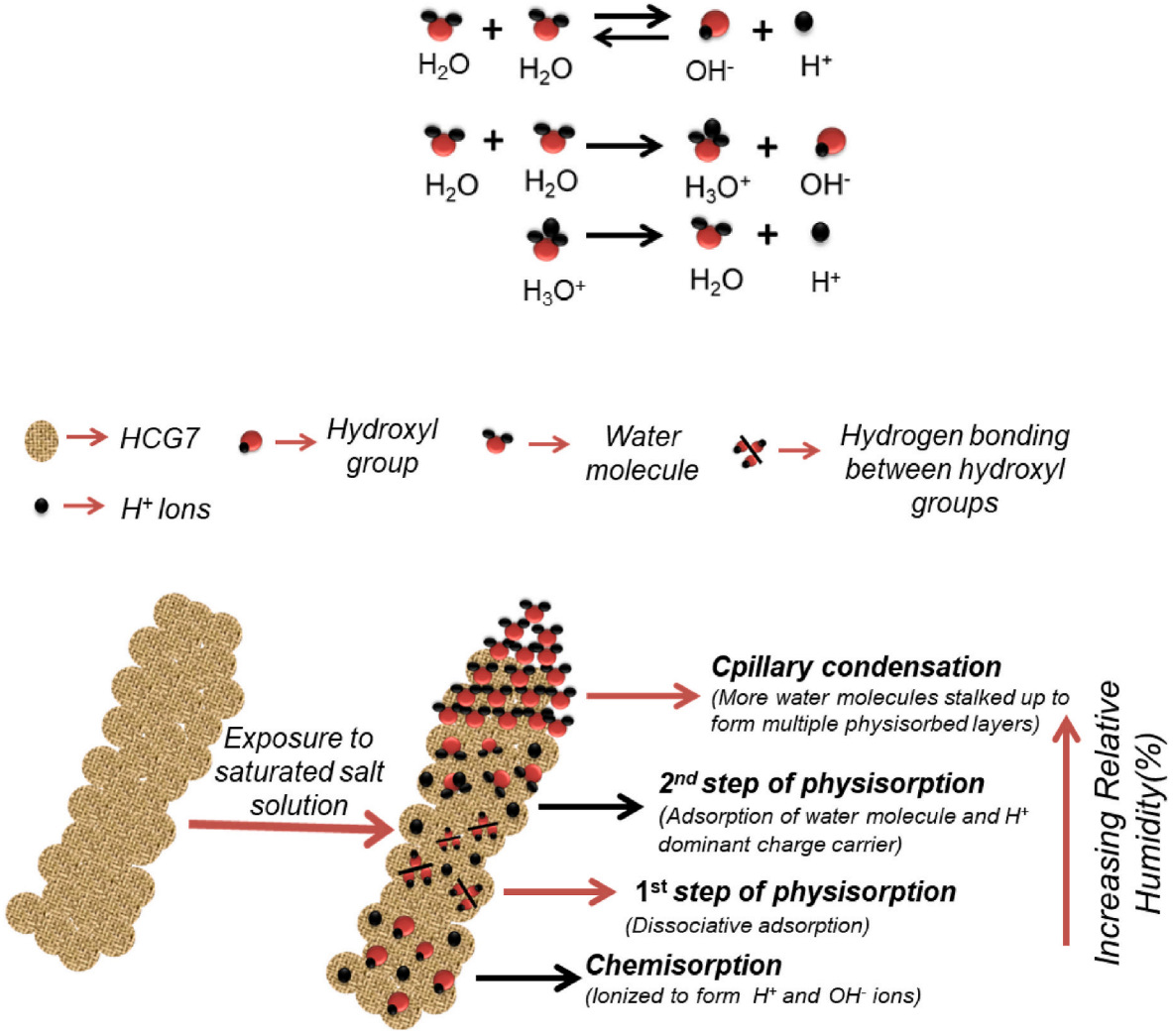

Fig. 6. Schematic of humidity sensing mechanism in CeO_2-GO composite.

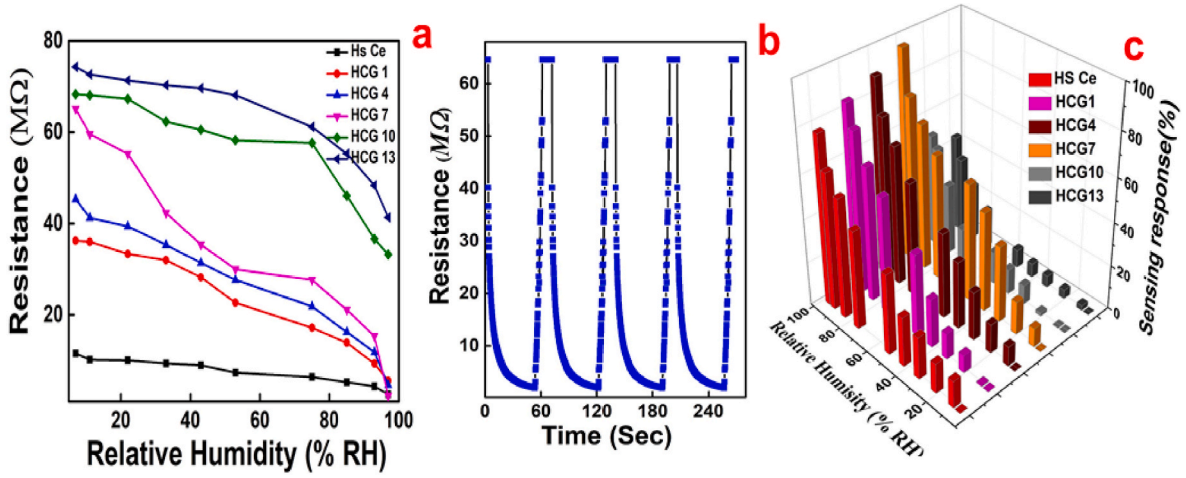

Fig. 7. Plot of (a) Resistance fluctuation as a function of relative humidity,(b)Response and recovery characteristics of HCG7,(c)Changes in sensing behaviour with respect to relative humidity.

condensation. In the first stage at low relative humidity levels water molecules are chemically adsorb on the sensor material and then gradually dissociate into OH and H^+ ions [6,70].Due to the hydrophilic groups that are present in the composite, as shown by FTIR investigations, when water molecules initially approach the sensing site, OH^- ions get chemisorbed onto the composite surface to form the first chemisorbed layer. H^+ ions then become mobile, causing a decrease in the composite's resistance. When there is an increase in humidity the

Table 3
Comparison of the current system's humidity sensing performance with certain earlier reports.

System	Response time (s)	Recovery time (s)	Reference
Ceria nanoroads	19	49	[23]
Ce dopped nanoporousZnO	13	17	[74]
Turncated octahedral CeO_2	10	14	[27]
Aero-gel based CeO_2nano particle	4.6	2.7	[75]
Graphene oxide	10.5	41	[76]
G/SnO_x/CFs	8	6	[77]
GO/NWF	8.9	11.76	[78]
Graphene/TiO_2	128	68	[79]
ZnO/rGO/Cu	19	42	[80]
HCG7	19	10	Present work

formation of the first physisorbed layer is also realised, as a result of hydrogen bonding between each water molecule and two nearby hydroxyl groups thus forming the immobile layer [71]. With subsequent increases in relative humidity, water molecules are simply adsorbed to the physisorbed layer and become mobile as a result, generating a second physisorbed layer. Such physisorbed layers were accumulated as the relative humidity rises and finally act like bulk liquid water. The images below shows the way the layers are generated. At this stage, each water molecule joins with each OH group to create H_3O^+, which then dissociates into H_2O and H^+ ions, according to Grotthus's mechanism [70,71]. As a result, the concentration of H^+ ions increase quickly, becoming mobile and hopping from one water molecule to the next by the simultaneous cleavage of the hydrogen bond network of the water molecules and the covalent bonds of nearby molecules [72].Further increase in relative humidity causes water to condense in the composites interlayer's, which finally allows for electrolytic conduction by further reduction of, and causing an increase in sensing response. The sensing strategy is represented in Fig. 6.

5.2.1. Humidity response and recovery behaviour

Response and recovery times, hysteresis, and stability are essential factors for fabricating an effective and reliable humidity sensing device. Two distinct chambers, one with a lower relative humidity (RH) of 11 % and another with a higher RH of 97 %, were maintained to allow for the precise experimental assessment of the response and recovery periods of all the samples. In a typical procedure for measure each sample was subjected humidity exposure ranging from 11 % RH to 97 % RH, and the conditions were retraced from 97 % RH to 11 % RH, respectively, keeping the switching duration 1 s [73].Resistance variation of different systems with change in humidity is provided in Fig. 7a. Among the systems investigated, HCG7 is identified as the best one in their response towards humidity. The response and recovery times of HCG 7 is shown in Fig. 7b. The results show that HCG7 sample has an excellent response time of 19 s and a quick recovery time of 10 s. Changes in sensing behaviour with respect to relative humidity is presented in Fig. 7c. It can be seen that the composite exhibits attractive response when compared to either of the two constituents alone. Though GO exhibited response time 10 s, the recovery time was rather high, 40 s. Incorporation of high surface area ceria has significantly reduced the response time, which at the optimum ceria amount is 10 s. Table 3 compares the sensor response of the system with those of other composites under comparable situations. A comparison of the result with data presented shows that the system can compete with other reported ones in terms of recovery time. However, response time was more attractive for other systems. Though pure ceria shows a good performance, the stability aspect makes the candidate less preferable. Despite the fact that that G/SnO_x/CFs reported attractive values of test parameters, the tedious synthesis pathway is pointed out as a demerit of the system. Hence, a comparison reveals that present work benefited by simple sample preparation conditions and the attractive recovery time is promising one in the field of humidity sensing.

5.2.2. Adsorption desorption hysteresis and stability

The variation of resistance of the system during adsorption and desorption of water vapour shows the hysteresis curve, which can be taken as a measure of performance of the material [71]. The area of hysteresis marks the efficiency. The experiments conducted using HCG7 is depicted in Fig. 8a.The hysteresis pattern of the composite shows that the adsorption process is spontaneous whereas the desorption process is delayed.This is because adsorption, which occurs in the humidity sensing situation, is an exothermic process and desorption, which occurs in endothermic manner. Comparatively low area validates the low recovery tome shown by the system.In order to test the stability of the composite as a humidity sensor, Sensing response of HCG7 for 60 days was examined at 33 % relative humidity and 97 % relative humidity and the corresponding graphs are displayed in Fig. 8b.As can be seen, HCG7 demonstrated high stability and stable sensing over the course of two months, establishing the system to be ideal for device manufacturing.

6. Conclusion

In this work, we have successfully addressed the shortcomings of CeO_2 and GO as a standalone humidity sensor by combining their qualities by synthesising their composite in various percentages using a straightforward hydrothermal technique. From the composites we created, HCG7 containing 7 wt% GO in ceria, has demonstrated an impressive sensing response of 99.93 % in the region of 11 %–97 % RH in addition to a very strong response time of 19 s and recovery time of 10 s. Additionally, the composite sensor has shown to be extremely stable with little hysteresis. Thus, the system offers the possibility of creating an effective, affordable, and humidity-sensing device that operates at room temperature. All of the aforementioned characteristics, together with the ease of fabrication and adaptability of the fabrication

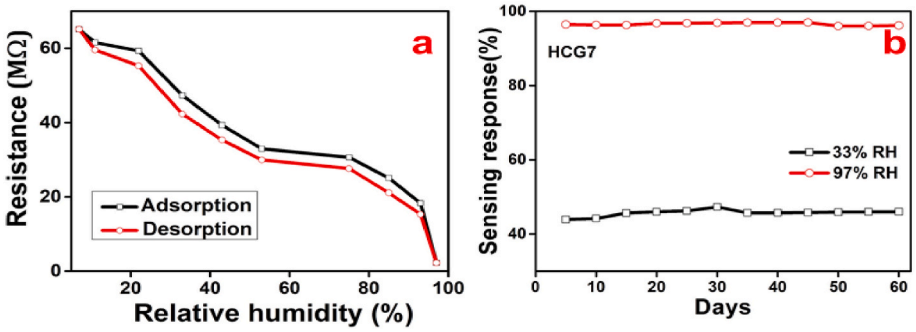

Fig. 8. (a) Humidity hysteresis of HCG7 and (b) Humidity sensing stability of HCG7.

process used to synthesise any other metal oxide, make this type of device a possible candidate for high performance and quick humidity sensor development.

CRediT authorship contribution statement

C Anjali: Investigation, Writing – original draft. **V Nidhisha:** Methodology. **T.P Amrutha:** Methodology. **Ritu Gopal:** Methodology. **B Chethan:** Resources. **Mohamed Shahin Thayyil:** Resources. **Pradeepan Periyat:** Resources. **Renuka Neeroli Kizhakayil:** Conceptualization, Supervision, Writing – original draft.

Declaration of competing interest

The authors declare that they have no known competing financial interests or personal relationships that could have appeared to influence the work reported in this paper.

Data availability

Data will be made available on request.

Acknowledgements

Anjali C. acknowledges Govt. of Kerala for the financial assistance through E Grant. The authors acknowledge CSIF, University of Calicut for providing the analytical facilities.

References

[1] S. Borini, R. White, D. Wei, M. Astley, S. Haque, E. Spigone, N. Harris, J. Kivioja, T. Ryhanen, ACS Nano 7 (2013) 11166–11173.
[2] J. Chu, X. Peng, P. Feng, Y. Sheng, J. Zhang, Sensor. Actuator. B Chem. 178 (2013) 508–513.
[3] Q.-Y. Tang, Y. Chan, K. Zhang, Sensor. Actuator. B Chem. 152 (2011) 99–106.
[4] W.-P. Chen, Z.-G. Zhao, X.-W. Liu, Z.-X. Zhang, C.-G. Suo, Sensors 9 (2009) 7431–7444.
[5] T. Blank, L. Eksperiandova, K. Belikov, Sensor. Actuator. B Chem. 228 (2016) 416–442.
[6] Z. Chen, C. Lu, Sens. Lett. 3 (2005) 274–295.
[7] Z. Li, H. Zhang, W. Zheng, W. Wang, H. Huang, C. Wang, A.G. MacDiarmid, Y. Wei, J. Am. Chem. Soc. 130 (2008) 5036–5037.
[8] A. Sun, L. Huang, Y. Li, Sensor. Actuator. B Chem. 139 (2009) 543–547.
[9] Q. Kuang, C. Lao, Z.L. Wang, Z. Xie, L. Zheng, J. Am. Chem. Soc. 129 (2007) 6070–6071.
[10] H. Feng, C. Li, T. Li, F. Diao, T. Xin, B. Liu, Y. Wang, Sensor. Actuator. B Chem. 243 (2017) 704–714.
[11] W. Li, J. Liu, C. Ding, G. Bai, J. Xu, Q. Ren, J. Li, Sensors 17 (2017) 2392.
[12] R. Malik, V.K. Tomer, V. Chaudhary, M.S. Dahiya, A. Sharma, S. Nehra, S. Duhan, K. Kailasam, J. Mater. Chem. A 5 (2017) 14134–14143.
[13] M. Parthibavarman, V. Hariharan, C. Sekar, Mater. Sci. Eng. C 31 (2011) 840–844.
[14] X. Song, Q. Qi, T. Zhang, C. Wang, Sensor. Actuator. B Chem. 138 (2009) 368–373.
[15] B. Wang, L. Zhu, Y. Yang, N. Xu, G. Yang, J. Phys. Chem. C 112 (2008) 6643–6647.
[16] L. Li, Z. Du, T. Wang, Sensor. Actuator. B Chem. 147 (2010) 165–169.
[17] Q. Qi, T. Zhang, Q. Yu, R. Wang, Y. Zeng, L. Liu, H. Yang, Sensor. Actuator. B Chem. 133 (2008) 638–643.
[18] L. Gu, K. Zheng, Y. Zhou, J. Li, X. Mo, G.R. Patzke, G. Chen, Sensor. Actuator. B Chem. 159 (2011) 1–7.
[19] T. Ates, C. Tatar, F. Yakuphanoglu, Sensor Actuator Phys. 190 (2013) 153–160.
[20] S. Jagtap, K. Priolkar, Sensor. Actuator. B Chem. 183 (2013) 411–418.
[21] K. Narimani, F.D. Nayeri, M. Kolahdouz, P. Ebrahimi, Sensor. Actuator. B Chem. 224 (2016) 338–343.
[22] S. Kano, K. Kim, M. Fujii, ACS Sens. 2 (2017) 828–833.
[23] A. Younis, A. Loucif, Ceram. Int. 47 (2021) 15500–15507.
[24] X. Liu, R. Wang, T. Zhang, Y. He, J. Tu, X. Li, Sensor. Actuator. B Chem. 150 (2010) 442–448.
[25] Y. Li, C. Deng, M. Yang, Sensor. Actuator. B Chem. 165 (2012) 7–12.
[26] V. Khadse, S. Thakur, K. Patil, P. Patil, Sensor. Actuator. B Chem. 203 (2014) 229–238.
[27] T. Divya, M. Nikhila, M. Anju, T.A. Kusumam, A. Akhila, Y. Ravikiran, N. K. Renuka, Sensor Actuator Phys. 261 (2017) 85–93.
[28] V. Manikandan, S. Sikarwar, B. Yadav, R. Mane, Sensor Actuator Phys. 272 (2018) 267–273.
[29] A. Tripathy, S. Pramanik, A. Manna, S. Bhuyan, N.F. Azrin Shah, Z. Radzi, N.A. Abu Osman, Sensors 16 (2016) 1135.
[30] Y. Yao, W. Ma, IEEE Sensor. J. 14 (2014) 4078–4084.
[31] P.-G. Su, W.-C. Li, J.-Y. Tseng, C.-J. Ho, Sensor. Actuator. B Chem. 153 (2011) 29–36.
[32] X. Xiao, Q.-J. Zhang, J.-H. He, Q.-F. Xu, H. Li, N.-J. Li, D.-Y. Chen, J.-M. Lu, Sensor. Actuator. B Chem. 255 (2018) 1147–1152.
[33] R.M. Morais, M. dos Santos Klem, G.L. Nogueira, T.C. Gomes, N. Alves, IEEE Sensor. J. 18 (2018) 2647–2651.
[34] H. Park, S. Lee, S.H. Jeong, U.H. Jung, K. Park, M.G. Lee, S. Kim, J. Lee, Sensors 18 (2018) 921.
[35] Z. Zhuang, D. Qi, C. Ru, J. Pan, C. Zhao, H. Na, Sensor. Actuator. B Chem. 253 (2017) 666–676.
[36] M. Sajid, G.U. Siddiqui, S.W. Kim, K.H. Na, Y.S. Choi, K.H. Choi, Sensor Actuator Phys. 265 (2017) 102–110.
[37] Y. Tan, K. Yu, T. Yang, Q. Zhang, W. Cong, H. Yin, Z. Zhang, Y. Chen, Z. Zhu, J. Mater. Chem. C 2 (2014) 5422–5430.
[38] J. Zhao, N. Li, H. Yu, Z. Wei, M. Liao, P. Chen, S. Wang, D. Shi, Q. Sun, G. Zhang, Adv. Mater. 29 (2017) 1702076.
[39] D. Burman, S. Santra, P. Pramanik, P.K. Guha, Nanotechnology 29 (2018) 115504.
[40] R.K. Jha, P.K. Guha, Nanotechnology 27 (2016) 475503.
[41] H. Guo, C. Lan, Z. Zhou, P. Sun, D. Wei, C. Li, Nanoscale 9 (2017) 6246–6253.
[42] D. Zhang, Y. Cao, P. Li, J. Wu, X. Zong, Sensor. Actuator. B Chem. 265 (2018) 529–538.
[43] P. Yasaei, A. Behranginia, T. Foroozan, M. Asadi, K. Kim, F. Khalili-Araghi, A. Salehi-Khojin, ACS Nano 9 (2015) 9898–9905.
[44] S.Y. Cho, Y. Lee, H.J. Koh, H. Jung, J.S. Kim, H.W. Yoo, J. Kim, H.T. Jung, Adv. Mater. 28 (2016) 7020–7028.
[45] J. Miao, L. Cai, S. Zhang, J. Nah, J. Yeom, C. Wang, ACS Appl. Mater. Interfaces 9 (2017) 10019–10026.
[46] J. Meng, T. Liu, C. Meng, Z. Lu, J. Li, Microporous Mesoporous Mater. (2023) 112663.
[47] G. Zhou, J.-H. Byun, Y. Oh, B.-M. Jung, H.-J. Cha, D.-G. Seong, M.-K. Um, S. Hyun, T.-W. Chou, ACS Appl. Mater. Interfaces 9 (2017) 4788–4797.
[48] J. Yeow, J. She, Nanotechnology 17 (2006) 5441.
[49] S.S. Varghese, S. Lonkar, K. Singh, S. Swaminathan, A. Abdala, Sensor. Actuator. B Chem. 218 (2015) 160–183.
[50] E. Singh, M. Meyyappan, H.S. Nalwa, ACS Appl. Mater. Interfaces 9 (2017) 34544–34586.
[51] Y. Gu, H. Jiang, Z. Ye, N. Sun, X. Kuang, W. Liu, G. Li, X. Song, L. Zhang, W. Bai, X. Tang, Electron. Mater. Lett. 16 (2020) 61–71.
[52] P. Singh, S. Shukla, Surface. Interfac. 18 (2020) 100410.
[53] V. Manikandan, I. Petrila, S. Vigneselvan, A. Mirzaei, R.S. Mane, S.S. Kim, J. Chandrasekaran, J. Mater. Sci. Mater. Electron. 31 (2020) 8815–8824.
[54] D.R. Dreyer, A.D. Todd, C.W. Bielawski, Chem. Soc. Rev. 43 (2014) 5288–5301.
[55] T. Daio, T. Bayer, T. Ikuta, T. Nishiyama, K. Takahashi, Y. Takata, K. Sasaki, S. Matthew Lyth, Sci. Rep. 5 (2015) 11807.
[56] H. Chi, Y.J. Liu, F. Wang, C. He, ACS Appl. Mater. Interfaces 7 (2015) 19882–19886.
[57] N. Zaaba, K. Foo, U. Hashim, S. Tan, W.-W. Liu, C. Voon, Procedia Eng. 184 (2017) 469–477.
[58] M.E. Khan, M.M. Khan, M.H. Cho, Sci. Rep. 7 (2017) 5928.
[59] T. Sen, N.G. Shimpi, S. Mishra, R. Sharma, Sensor. Actuator. B Chem. 190 (2014) 120–126.
[60] S.A. Ansari, M.M. Khan, M.O. Ansari, S. Kalathil, J. Lee, M.H. Cho, RSC Adv. 4 (2014) 16782–16791.
[61] M. Bera, P. Gupta, P.K. Maji, J. Nanosci. Nanotechnol. 18 (2018) 902–912.
[62] A.A. Ansari, J. Semiconduct. 31 (2010) 053001.
[63] M.E. Khan, M.M. Khan, M.H. Cho, J. Colloid Interface Sci. 482 (2016) 221–232.
[64] F.T. Johra, J.-W. Lee, W.-G. Jung, J. Ind. Eng. Chem. 20 (2014) 2883–2887.
[65] A. Khort, V. Romanovski, V. Lapitskaya, T. Kuznetsova, K. Yusupov, D. Moskovskikh, Y. Haiduk, K. Podbolotov, Inorg. Chem. 59 (2020) 6550–6565.
[66] H. Huang, D. Li, Q. Lin, W. Zhang, Y. Shao, Y. Chen, M. Sun, X. Fu, Environ. Sci. Technol. 43 (2009) 4164–4168.
[67] T. Saravanan, M. Shanmugam, P. Anandan, M. Azhagurajan, K. Pazhanivel, M. Arivanandhan, Y. Hayakawa, R. Jayavel, Dalton Trans. 44 (2015) 9901–9908.
[68] S. Rajendran, M.M. Khan, F. Gracia, J. Qin, V.K. Gupta, S. Arumainathan, Sci. Rep. 6 (2016) 31641.
[69] M.J. Islam, D.A. Reddy, J. Choi, T.K. Kim, RSC Adv. 6 (2016) 19341–19350.
[70] D. Zhang, D. Wang, P. Li, X. Zhou, X. Zong, G. Dong, Sensor. Actuator. B Chem. 255 (2018) 1869–1877.
[71] W.-D. Lin, H.-M. Chang, R.-J. Wu, Sensor. Actuator. B Chem. 181 (2013) 326–331.
[72] Q. Chen, M. Nie, Y. Guo, Sensor. Actuator. B Chem. 254 (2018) 30–35.
[73] M.V. Fuke, P. Kanitkar, M. Kulkarni, B. Kale, R. Aiyer, Talanta 81 (2010) 320–326.
[74] M. Anbia, S.E.M. Fard, J. Rare Earths 30 (2012) 38–42.
[75] E. Poonia, P.K. Mishra, V. Kiran, J. Sangwan, R. Kumar, P.K. Rai, R. Malik, V. K. Tomer, R. Ahuja, Y.K. Mishra, J. Mater. Chem. C 7 (2019) 5477–5487.
[76] H. Bi, K. Yin, X. Xie, J. Ji, S. Wan, L. Sun, M. Terrones, M.S. Dresselhaus, Sci. Rep. 3 (2013) 2714.
[77] T. Fu, J. Zhu, M. Zhuo, B. Guan, J. Li, Z. Xu, Q. Li, J. Mater. Chem. C 2 (2014) 4861–4866.
[78] Y. Wang, L. Zhang, Z. Zhang, P. Sun, H. Chen, Langmuir 36 (2020) 9443–9448.
[79] W.-D. Lin, C.-T. Liao, T.-C. Chang, S.-H. Chen, R.-J. Wu, Sensor. Actuator. B Chem. 209 (2015) 555–561.
[80] D. Kuntal, S. Chaudhary, A. Kiran Kumar, R. Megha, C.V. Ramana, Y. Ravi Kiran, S. Thomas, D. Kim, J. Mater. Sci. Mater. Electron. 30 (2019) 15544–15552.